npj | 2D materials and applications

Article

Published in partnership with FCT NOVA with the support of E-MRS

https://doi.org/10.1038/s41699-024-00490-9

Emergence of polar skyrmions in 2D Janus $CrInX_3$ (X=Se, Te) magnets

Fengyi Zhou[1], Monirul Shaikh[2], Weiwei Sun[3], Feng Chen[1], Xin Chen[4], Shu Li[1], Henry Tong[1], Biplab Sanyal[5] ✉ & Duo Wang[1] ✉

In the realm of multiferroicity in 2D magnets, whether magnetic and polar skyrmions can coexist within a single topological entity has emerged as an important question. Here, we study Janus 2D magnets $CrInX_3$ (X=Se, Te) for a comprehensive investigation of the magnetic ground state, magnetic excited state, and corresponding ferroelectric polarization by first-principles electronic structure calculations and Monte Carlo simulations. Specifically, we have thoroughly elucidated the magnetic exchange mechanisms, and have fully exemplified the magnetic field dependence of the magnon spectrum. More importantly, our study reveals a previously unrecognized, remarkably large spin-spiral-induced ferroelectric polarization (up to 194.9 $\mu C/m^2$) in both compounds. We propose an approach to identify polar skyrmions within magnetic skyrmions, based on the observed direct correlation between spin texture and polarization density. Elucidating this correlation not only deepens our understanding of magnetic skyrmions but also paves the way for innovative research in the realm of multiferroic skyrmions.

Topological magnetic states are non-trivial magnetic structures. Based on their specific swirling configurations of spins, which can be characterized by topological charge number, they are classified as skyrmions, biskyrmions, merons, vortices, etc[1–5]. These topological spin configurations have received the most attention in recent years due to their intriguing electromagnetic properties, such as extraordinarily low current-driven threshold and highly efficient motion dynamics[6]. These effective interactions between electric fields (or currents) and the specific spin states enable materials to exhibit fascinating phenomena, such as the topological Hall effects[7], spin transfer torque[6,8], and spin-orbit torque[9]. These novel magneto-electric properties combined with their particle-like size and exceptional topological protected stability make the materials promising potential for applications in spintronics[10] and orbitronics[11], particularly in high-density magnetic storage devices[12].

Another effective way of electric control involves the use of magneto-electric multiferroics. The search for these materials is driven by the prospect of controlling charges by applied magnetic fields and spins by applied voltages, thereby constructing new forms of multifunctional devices[13–15]. However, the performance of currently found multiferroic materials is still far from satisfying practical applications. The primary limiting factors are twofold: (i) the weak magnetoelectric coupling, and (ii) the operation temperature is substantially below room temperature. It is because ferroelectricity and magnetism tend to be mutually exclusive with each other when coexist, which is dictated by the nature of their respective d-electron occupations[16]. Whereas in an ideal multiferroic material, the dipolar order should be directly coupled to long-range magnetic configuration. One intriguing mechanism perfectly satisfies the requirement, in which the dipole moment is induced by having some specific patterns of non-collinear spin state. As a result, ionic displacement at the ligand site has been activated, and therefore, ferroelectric polarization is induced (the so-called inverse Dzyaloshinsky-Moriya mechanism)[17]. Typical types of spin texture that exhibit this dipole order include the well-studied Néel-type domain wall[18], and more notably, the magnetic skyrmions, which have recently received widespread attention. Several experimental results have already shown the existence of multiferroic properties in magnetic skyrmions. For example, in GaV_4S_8[19], the ferroelectric polarization undergoes interesting changes along with the magnetic phase transition from a cycloidal order to Néel-type skyrmions. The polarization results deduced on Cu_2OSeO_3 indicate that each magnetic skyrmion locally carries an electric dipole or quadrupole moment[20,21]. Recently, an interesting theoretical study reported spin-chirality-drive multiferroicity in vanadium-halid compounds[22]. However, questions such as the relationship between the magnetic topological feature and the electric polarization, the precise manifestation of the polarization density, the potential role of this phenomenon as the origin of

[1]Faculty of Applied Sciences, Macao Polytechnic University, Macao SAR, 999078, China. [2]Department of Physics and Astronomy, University of Nebraska, Kearney, NE, 68849-1160, USA. [3]SEU-FEI Nano-Pico Center, Key Laboratory of MEMS of Ministry of Education, School of Electronic Science and Engineering, Southeast University, Nanjing, 210096, China. [4]Thermal Science Research Center, Shandong Institute of Advanced Technology, Jinan, 250100, China. [5]Department of Physics and Astronomy, Uppsala University, Uppsala, 75120, Sweden. ✉e-mail: biplab.sanyal@physics.uu.se; duo.wang@mpu.edu.mo

polar skyrmions, and the design strategies for generating multiferroic skyrmion with robust magneto-electric coupling at high temperatures, remain unanswered. To effectively address these issues, comprehensive and systematic theoretical studies based on the first-principles methods are a necessity.

Compared to bulk materials, low-dimensional materials, due to their broken symmetry, become an ideal platform for the emergence of numerous excellent properties and even new physical phenomena. The same for the study of magnetic skyrmions. Both experimental and theoretical studies have shown that a variety of magnetic topological states exist in low-dimension systems, such as Néel-type skyrmions in Fe/Ir(111)[23], mixed Bloch-Néel skyrmions in Co/Pd multilayers[24], bimerons in a thin plate of $Co_8Zn_9Mn_3$[25], etc. Janus structure is an important member of 2D functional materials. Until now, most synthesized Janus 2D materials exhibit Janus characteristics due to anions asymmetrically occupying opposite surfaces, such as MoSSe[26,27] and WSSe[28], which can be prepared by modified chemical vapor deposition. Recently, a mechanically force-assisted synthesis of GeSe has been achieved[29], and more cation-characterized Janus 2D materials are expected to be synthesized using unconventional synthesis methods such as pulsed laser deposition (PLD)[30,31], and high-pressure and high-temperature apparatuses[32]. At the same time, there have been extensive theoretical studies on such materials[26,27,33–40]. Among them, monolayer $CrInSe_3$ and $CrInTe_3$ are exceptional examples[39]. These compounds are derived from van der Waals material In_2Se_3 that has been proven to exhibit room-temperature ferroelectricity with reversible spontaneous electric polarization[41–43]. With Cr partially substituted at the In site, $CrInX_3$ are predicted to be stable and exhibit spontaneous magnetic skyrmions. However, the physical mechanism behind the magnetic exchange coupling remains to be fully understood. A thorough investigation, particularly into their magnetic ground state and excited state, is still required. More importantly, the intriguing possibility of multiferroicity, especially the presence of multiferroic skyrmions, remains unexplored.

In this paper, the magnetic properties of monolayer $CrInSe_3$ and $CrInTe_3$ are thoroughly investigated, starting with obtaining a rank-2 exchange matrix. The isotropic Heisenberg exchange J is analyzed by combining orbital-decomposed coupling results and electronic properties in specific local CrX_6 crystal field. The antisymmetric Dzyaloshinskii-Moriya vector $\mathbf{D}_{ij}$ is obtained and its mechanism is explained by intriguing variation of spin-orbit coupling strength on different X layers. Macroscopic magnetic studies on the two systems are conducted by investigating magnetic equilibrium states under various external temperatures and magnetic field perturbations. These magnetic structures are then used as input for studying the spin wave spectrum and consequently, a complete picture of magnetic properties from the ground state to the excited state is achieved. In addition, spontaneous electric polarization values are obtained by using both the modern theory of polarization and the phenomenological Landau treatment. By analyzing polarization densities calculated from various magnetic structures, we further conclude a direct correlation between electric polarization and the combined effects of topological magnetic state, non-magnetic ligand atoms, external magnetic field, and temperature. Based on which, the possibility of having a multiferroic skyrmion is also discussed.

Results and discussion

Structural model and ground state properties in the collinear limit

Monolayer $CrInX_3$ is a Janus material consisting of five atomic layers and belongs to the C_s point group. As it is shown in Fig. 1b, indium atoms are situated on the upper side, with four nearest white ligand X atoms forming a tetrahedron structure. On the bottom side, a chromium layer is sandwiched between two layers of X atoms. Each chromium atom and its six nearest X neighbors form an octahedron. These two parts are connected by a shared X layer in the middle, which causes both the InX_4 tetrahedron and the CrX_6 octahedron to be slightly distorted from their ideal local structures. The dynamic and thermal stability of monolayer $CrInX_3$ has been theoretically validated by the phonon spectra and ab initio molecular dynamic simulations[39]. Moreover, the stability of $CrInX_3$ is further demonstrated by comparing its formation energies to those of the already synthesized parent compounds, monolayer In_2X_3, as shown in Supplementary Table 1.

In order to determine the most stable magnetic structure, our studies were first performed in the collinear framework. Four different magnetic states are considered in our ab initio calculations. As is shown in Fig. 2, these include one ferromagnetic (FM) configuration, and three antiferromagnetic (AFM) configurations with parallel spin chains along **a, b**, and **a**+**b** direction, respectively. The results are shown in Supplementary Table 2. For both Se- and Te-based compounds, the structure with the lowest energy appears with the FM state. The three structures with different AFM patterns exhibit higher energy, all with exactly the same amount (~0.40eV), suggesting equivalence regardless of the three directions of the parallel spin chain. Compared to the Te-based compound with a lattice constant of 8.56 Å, the Se-based compound exhibits a shorter one at 7.92 Å. Moreover, the Se-based compound exhibits a bigger energy difference between FM and AFM states(~0.02eV). These characteristics suggest a stronger exchange coupling in the Se-based compound, as will be discussed in detail in Section "Inter-site magnetic exchange interactions and their mechanisms".

Moreover, when comparing the Cr-Cr distance along the directions with FM and AFM spin chains, it is found that the Cr-Cr pair with parallel spins (3.96 Å and 4.28 Å) is larger than those with antiparallel spins (3.95 Å and 4.26 Å). This provides evidence that the crystal structure is affected by the changes in magnetic configuration. The phenomenon is called magnetostriction, or spin-lattice coupling. By further comparing the Cr-Cr distance change in the two materials, we found that the value for the Te-based compound (0.02 Å) is doubled compared to the Se-based one (0.01 Å). This suggests a stronger magnetostriction and, consequently, a generally larger ionic displacement in the Te-based compound when the material's magnetic configuration changes. In addition, as the magnitude of displacement is directly dictated by the relative orientations of the neighboring spin pairs, the lattice patterns in a material with complex spin textures, such as spin spiral or magnetic skyrmions, are expected to have various interesting features as well. These lattice patterns will then induce the positive and negative charges to be off-centered, which in turn induces ferroelectric polarization. Detailed discussions of ferroelectric polarization properties and direct magneto-electric coupling in these compounds will be addressed in Section "Complex ferroelectric polarization properties".

The electronic band structure and density of states (DOS) for the two systems are shown in Fig. 3. The electronic bands for both systems exhibit similar features. Specifically, in the spin-up channel, the lowest unoccupied bands are strongly hybridized by all three atoms in the system. Among these, the contribution from the transition metal Cr atom is slightly larger than the others. The highest occupied bands are mainly contributed by the ligand Se and Te states. As a result, these features give rise to bandgaps of 0.75 eV and 0.18 eV for the two compounds. In the spin-down channel, the unoccupied states are primarily from the In and the same ligand. Similar to the other channel, the bands just below the Fermi level are largely occupied by these ligand states. The overall bandgap is dictated by the feature exhibited in the spin-up channel.

To determine the magnetocrystalline anisotropy energy (MAE), total energies with spins along [100], [010], and [001] are calculated. As it is revealed in Supplementary Fig. 1, the easy-magnetization axes of $CrInSe_3$ and $CrInTe_3$ are both out-of-plane. Moreover, $CrInTe_3$ exhibits stronger anisotropy energy than $CrInSe_3$, which reflects the strength of spin-orbit coupling of Te, and Se atoms.

Inter-site magnetic exchange interactions and their mechanisms

In the ideal ionic picture, the charge state of Cr in this material is 3+, yielding a $3d^3$ electronic configuration. Due to the octahedral crystal field environment, the d orbital splits into a twofold degenerate high-energy e_g level and a three-fold degenerate low-energy t_{2g} level. As a result of intra-atomic Hund's interaction, the latter one is half-filled, resulting in a triplet S=3/2 state, which gives the moment of 3 Bohr magneton. The calculated moments for the two compounds, each with four different magnetic configurations, are shown in Supplementary Table 2. The first observation is that the moments

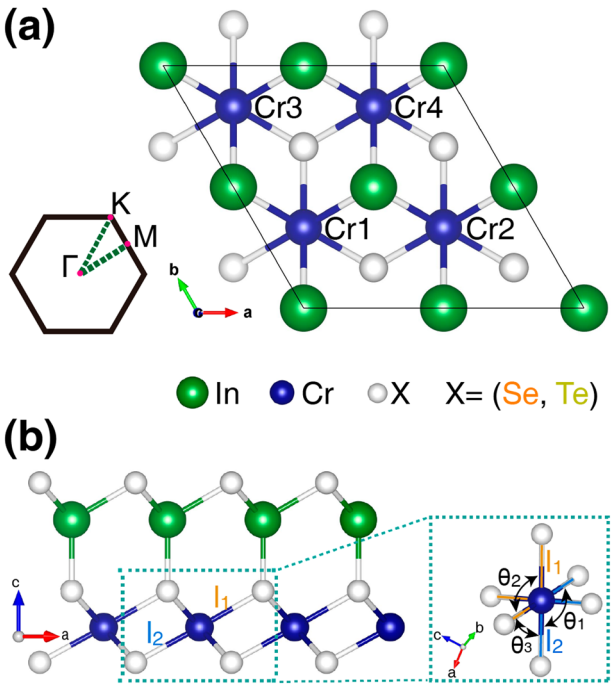

Fig. 1 | Structural model of CrInX_3 (X=Se, Te). a Top view and first Brillouin zone with specific high symmetry points, **b** side view and a schematic picture of local CrX_6 octahedron. Cr, In, X atoms are represented by blue, green, and white spheres, respectively.

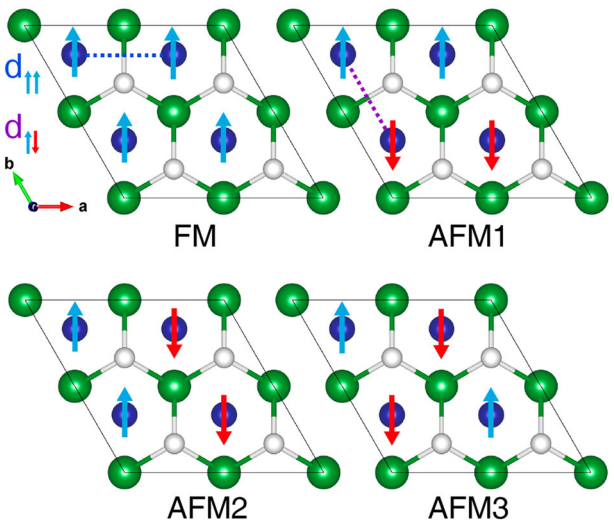

Fig. 2 | Four collinear magnetic structures are considered in this work. Cyan and red arrows indicate the orientations of spins on specific Cr atoms. Dashed lines in blue and purple represent two different nearest Cr-Cr distances due to parallel or antiparallel magnetic interactions.

range from 3.44 to 3.53 μ_B for $CrInSe_3$, and from 3.64 to 3.71 μ_B for $CrInTe_3$. These minor variations confirm the localized character of the Cr-d electrons, thereby validating the legitimacy of the Heisenberg model for accurately describing this system, as adopted in this paper. The second, and more significant observation, is that the calculated moments for the two compounds are noticeably larger—between 0.44 and 0.71 μ_B—than the values predicted from the above-described ideal picture. The moment deviation can often be attributed to local structural distortions or to electronic hybridization. As will be discussed in the following, this additional amount of electron plays a crucial role in determining electronic occupation, orbital structure, and consequently, the exchange routes. The three elements, in addition, serve as important factors in elucidating the magnetic exchange mechanism.

As shown in Fig. 1b, the octahedra exhibits distortion due to its Janus nature, characterized by two Cr-X bond lengths and three X-Cr-X bond angles. As the detailed data is listed in Supplementary Table 3, the differences in bond length are less than 0.22 Å, and the bond angles deviate from 90° by approximately 8°. This relatively minor distortion indicates that one can assuredly investigate the exchange mechanism and electron occupation within a standard octahedral crystal field. Schematic picture of the first three inter-site exchange pairs and the isotropic exchange parameters as a function of distance are plotted in Fig. 4a. The first observation is that the J values decrease rapidly as the Cr-Cr distance increases. Specifically, only the first-nearest and third-nearest couplings make a noticeable contribution to the system. Take $CrInSe_3$ as an example, the magnitude of the first nearest FM coupling is more than nineteen times bigger than the third nearest AFM coupling, with values of 7.39 and –0.37 meV, respectively. This results explains why systems show a strong inclination towards an FM ground state in the collinear limit. By incorporating orbital information into the on-site potential and the inter-site Green's function in the LKAG formula, one can obtain the orbital-resolved exchange parameters. In an octahedral crystal structure, the total exchange parameter (black lines) is contributed by the coupling from three different orbital channels: t_{2g}-t_{2g} (red lines), e_g-e_g (blue lines), and t_{2g}-e_g (green lines). And overall exchange coupling for any specific Cr-Cr pair is determined by the competition among the three. Taking the first nearest J_{tot} as an example, it is decomposed to competition between a significant positive t_{2g}-e_g coupling (9.12 meV) and a substantially negative e_g-e_g coupling (-1.39 meV), while the other one, t_{2g}-t_{2g}, keeps almost zero (-0.35 meV).

To understand this coupling pattern, it's necessary to clarify the physical nature of the electronic occupation, as well as the orbital states in the systems. For these compounds, the electronic quantities must be projected from the global Cartesian coordinates into a more physically meaningful, local octahedral basis. Figure 4b and Supplementary Table 4 present the lm-decomposed DOS and the respective DOS integration up to the Fermi level. After the rotation, a three-fold t_{2g} degeneracy and a twofold e_g degeneracy can be clearly seen in the DOS. Due to the strong hybridization, the three states that belong to the lower energy t_{2g} level contain around 0.80 electrons each, and interestingly, the two states of the higher energy e_g level are occupied by more than 0.71 electrons each. As a result, it gives the Cr atom about 2.4 and 1.4 electrons for t_{2g} and e_g levels, respectively. This atypical e_g occupation is the direct reason for the system's remarkable t_{2g}-e_g and e_g-e_g couplings, as the exchange mechanism depicted in a schematic picture shown in Fig. 4c. The hopping of the form t_{2g}-e_g leads to an exchange coupling that is predominantly FM due to the local Hund's rule. The hopping of the form e_g-e_g is energy favorable with FM alignment, but due to the specific exchange pathway, $Cr_i(d_{x^2-y^2})$-$X(p_x)$-$Cr_j(d_{x^2-y^2})$, formed by the hopping of electrons from an occupied $d_{x^2-y^2}$ orbital at site i to an unoccupied $d_{x^2-y^2}$ orbital at site j through a $pd\sigma$ bonding state, it gives a sizable AFM contribution instead (detailed discussions in Supplementary Note 1). Additionally, the hopping of the form t_{2g}-t_{2g} is prohibited for FM alignment due to the already half-filled t_{2g} states on the other site. Therefore, a weak AFM coupling is shown in Fig. 4a. This unconventional exchange mechanism due to the e_g occupation was also confirmed in a previous study on monolayer CrI_3[44].

By comparing the dominant exchange coupling (J_1) in the two compounds, we find that the FM exchange coupling strength diminishes from 7.39 meV in the Se-based compound to 4.75 meV in the Te-based one. This is markedly influenced by the larger lattice constant in the Te-based compound. More fundamentally, it is directly dictated by the changes in orbital occupation, which in turn, alters the exchange pathways. In specific, as the number of electrons occupying e_g states increases from 1.25 to 1.34 in $CrInTe_3$ (as shown in Table 1), it exhibits stronger AFM e_g-e_g coupling and therefore, provides slightly more compensation for the dominant FM t_{2g}-e_g coupling.

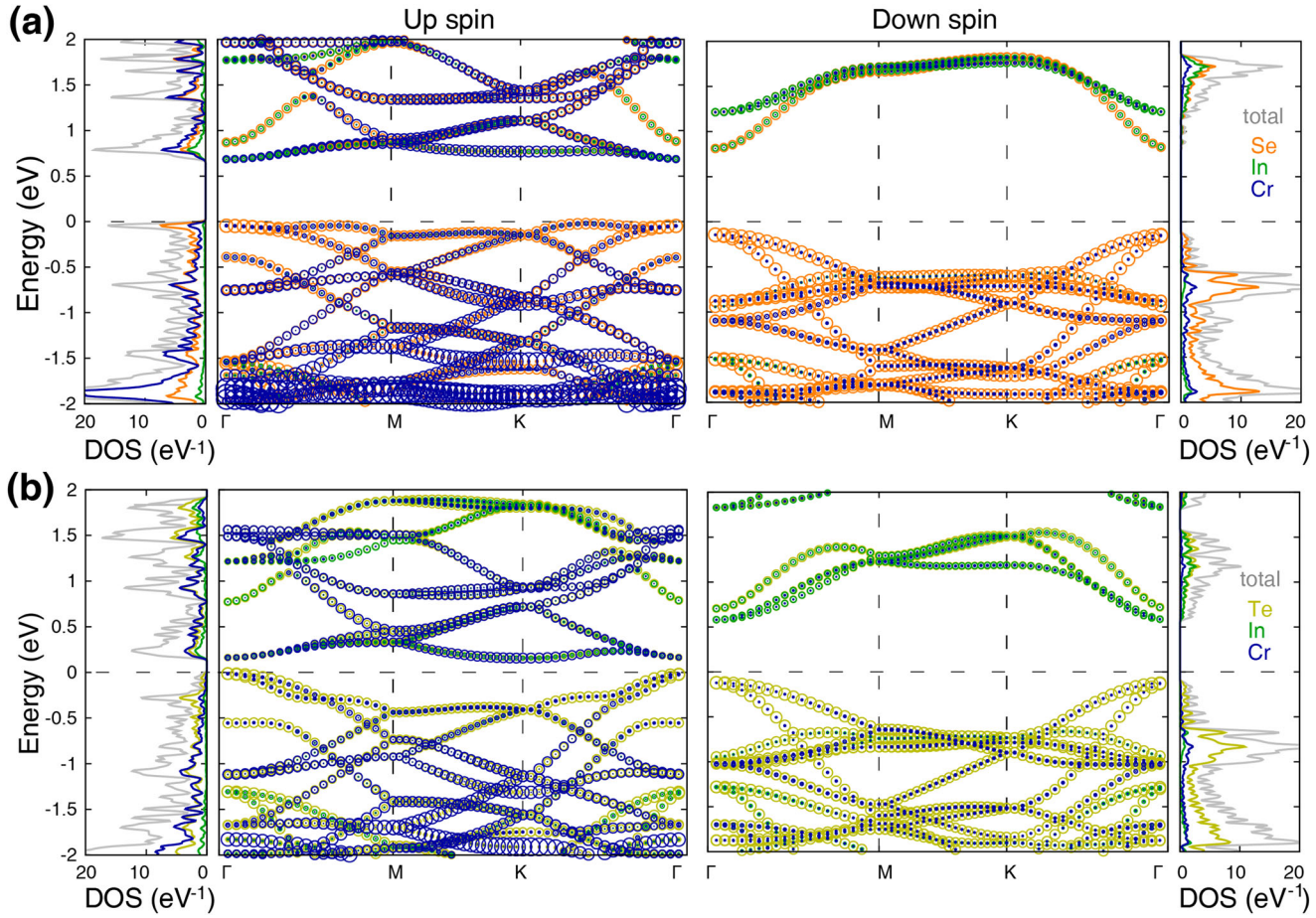

Fig. 3 | Electronic band structures and density of states (DOS). Atomic projected DOS and the electronic band structure for up-spin and down-spin electrons of **a** $CrInSe_3$ and **b** $CrInTe_3$ in the FM state are presented. Total DOS is shown in gray, and the atomic contributions of Cr, In, Se, and Te are shown in blue, green, orange, and olive curves (circles) in DOS (band structure), respectively. The size of the circles in band structure is proportional to the contribution weight. The Fermi level is set to 0 eV.

In systems where spin-orbit coupling plays an unignorable effect, the off-diagonal elements in Eq. (2) become non-zero. In some cases, the elements in the matrix are not exactly symmetric, from which a non-zero vector can be derived. This three-dimensional (3D) vector, stemming from the aforementioned time-reversal symmetry breaking, is known as the Dzyaloshinskii-Moriya (DM) vector, and the corresponding interaction is referred to as DM interaction. In contrast to the Heisenberg exchange parameter which depicts the collinear magnetic coupling strength of the system, the DM vector is a key determinant of whether it is possible to show a non-linear magnetic structure. Therefore, how to understand them correctly is an essential question that must be addressed.

The emergence of DM interaction can be understood well by analyzing the symmetry elements in $CrInX_3$. As is illustrated in Supplementary Fig. 8a, b, DMI originates from the deviation of ligand atoms positioned relative to the midpoint of the nearest Cr-Cr pairs. Specifically, as the upward and downward atoms (Se_{up} and Se_{dn}) deviate from the positions of the pink atoms, the point group of the structure is reduced from D_{6h} to C_{3v}. This process involves the following four symmetry operation changes: 1. The disappearance of the mirror plane perpendicular to the six-fold rotation axis; 2. The replacement of the six-fold rotation by a three-fold rotation axis; 3. The original six mirror planes parallel to the c-direction are reduced to three; 4. The disappearance of all the twofold rotation axes that were originally aligned with the six mirrors.

In addition, according to Moriya's symmetry rule[45], the orientation of this interaction is determined by the cross product of two vectors as per the equation $\mathbf{D}_{ij} \sim \boldsymbol{r}_{ij} \times \boldsymbol{a}$. Here, $\mathbf{r}_{ij}$ is a vector that connects the two magnetic atoms, and $\mathbf{a}$ represents the displacement of the ligand atom relative to the midpoint of the two magnetic atoms. Whereas in $CrInX_3$, the physical mechanism of DM vectors is more complex than what this simplified theory suggests. The calculated vectors of the nearest neighbor Cr-Cr pair are shown in Fig. 5a. Six vectors around each Cr atom exhibit (a slightly deviated) clockwise pattern. Upon examining the crystal structures, we found that each nearest Cr-Cr pair is connected by two ligand atoms, positioned in two different layers (as depicted by white and orange spheres in Fig. 5a). Therefore, two Cr-$X_{up|dn}$-Cr triangles are formed, and as a result, two vectors, which are proven to be in opposite directions, are generated. The overall DM vector between this specific Cr-Cr pair is determined by competition between the two. As DM interaction directly originates from the spin-orbit coupling effect of ligand atoms, a detailed analysis of MAE contribution is performed to further investigate this interaction mechanism. As shown in Fig. 5b, compared to all the other atoms, the ligand X at the bottom layer (X_{dn}) carries a majority of the spin-orbit effect into the system. As a result, the DM vector generated by the lower Cr-X_{dn}-Cr triangle is bigger than the other one and, therefore, plays a dominant role in determining the overall vector orientation. It is remarkable that the same atoms, merely due to their different positions, play entirely different roles in the MAE contribution. Subsequent investigation uncovered that the origin of this phenomenon lies in the different bonding environments of the X atoms in the two layers: the upper layer is connected to In atoms, while the lower layer is not. In addition, we measured the respective X_{dn} displacements relative to the midpoint of Cr-Cr pairs in $CrInSe_3$, as shown in Supplementary Fig. 8c. The values from d_1 to d_6 are listed in Supplementary Table 5. These six displacements can be classified into three categories: $d_1 = d_3$, $d_2 = d_4$, and $d_5 = d_6$. As a result, this breaks the C_3 rotational symmetry and

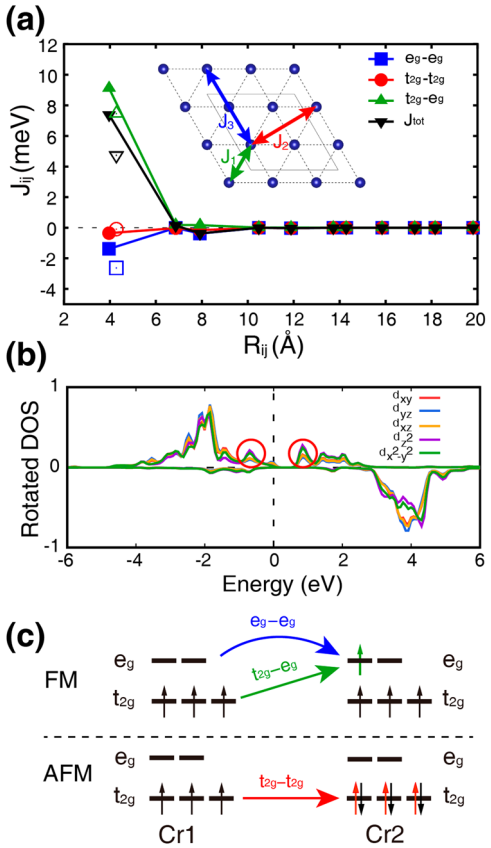

Fig. 4 | Heisenberg exchange parameters and corresponding exchange mechanism. a Orbital-decomposed exchange parameters plotted as a function of Cr-Cr distance, obtained for $CrInSe_3$ (solid points and lines) and $CrInTe_3$ (hollow points and only plotted the first-, second-, and third-nearest neighbor Cr-Cr pair), positive number indicates FM contribution, and negative means AFM. Inserts are Cr lattice of $CrInX_3$, the first-, second-, and third-nearest neighbor Cr-Cr pair are represented by green, rose red, and orange arrows, respectively. **b** The rotated DOS for decomposed 3*d* orbital of $CrInSe_3$ with the state of FM. **c** Schematic picture of orbital-dependent exchange mechanism.

reduces the three mirror planes to a single mirror plane that is diagonal to the system's unit cell, thereby giving the system a C_s point group, as illustrated in Fig. 5a.

On the other hand, it is relatively easy to understand the magnitude of the calculated DM vectors. In any of the two systems, the *X* atoms in each layer are equivalent, therefore, the size of the generated DM vector is the same. This specific displacement pattern provides $CrInX_3$ with a corresponding DMI symmetry (C_s). As the magnitudes of any two mirror-reflected DMI vectors are nearly identical, larger displacements of d_4 and d_2 result in greater magnitudes of these DMI vectors — 0.77 meV (shown as purple and yellow arrows in Supplementary Fig. 8c), compared to an average of 0.57 meV for the other displacements in $CrInSe_3$. When comparing the DM vectors in Se-based and Te-based compounds, it can be concluded that, with a heavier element in the system, the magnitude of the DM vector is bigger. As it is shown in Supplementary Table 6, $|\mathbf{D}_{ij}|$ in $CrInTe_3$ is approximately 2.4 times bigger than in $CrInSe_3$, with values of 1.86 and 0.77 meV, respectively.

Magnetic topological states and their equilibrium and excited states

To obtain the compound's dynamic properties on a relatively macroscopic scale under different external magnetic fields and temperatures, classic Monte Carlo simulations were carried out. Calculations were performed with 5 ensembles under the same conditions to illustrate the relative stability of different magnetic structures and to properly average the properties.

Table 1 | The integrated electrons number of d decomposed orbitals of $CrInX_3$ (*X*=Se, Te) with FM magnetic structure

		t_{2g}	e_g	d
	N_{up}	2.41	1.43	3.84
$CrInSe_3$	N_{dn}	0.19	0.18	0.37
	M	2.22	1.25	3.47
	N_{up}	2.46	1.49	3.94
$CrInTe_3$	N_{dn}	0.15	0.15	0.30
	M	2.30	1.34	3.64

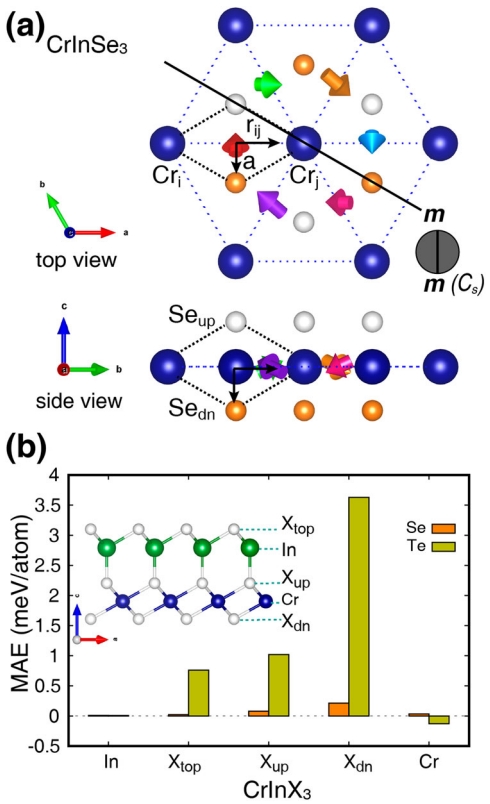

Fig. 5 | Dzyaloshinskii-Moriya interaction and the corresponding exchange mechanism. a Calculated DM parameters of the nearest neighbor bonds in $CrInSe_3$ compounds. White and orange spheres represent upper and lower layers of the ligand Se atoms, respectively. The direction and size of the DM vectors between specific Cr-Cr pairs are represented by colored arrows, with the length of arrow scaling with the DMI strength. **b** Calculated MAE contributions for each atom in $CrInX_3$ compounds.

Among them, the one with the lowest energy was considered as the ground state, leading to the phase diagrams shown in Fig. 6.

For the ground state at 0 K and 0 T, as shown at the left bottom corner of the phase diagram, both compounds show spin stripe texture. As can be seen in the side view (Fig. 6c, d), they exhibit clockwise spin helical configurations along specific real-space directions. Particularly, in $CrInSe_3$, the spin helical propagation is along the $[\sqrt{3}/2, 1/2, 0]$ direction (forming a 60° stripe-type domain) with a periodicity of 13.77 nm. With spin chains that are parallel to this direction having the exact same propagation pattern (as shown in the zoomed-in image in Fig. 6), this spin stripe state can be described by a single **q** vector. Whereas in $CrInTe_3$, the ground-state spin-spiral stripe is complex and cannot be characterized properly by a single propagation vector, a multi-q description with different propagation directions or periods is needed. Thereby a multi-**q** with a 40° stripe-type domain and a significantly smaller periodicity of 2.22 nm is formed. Given

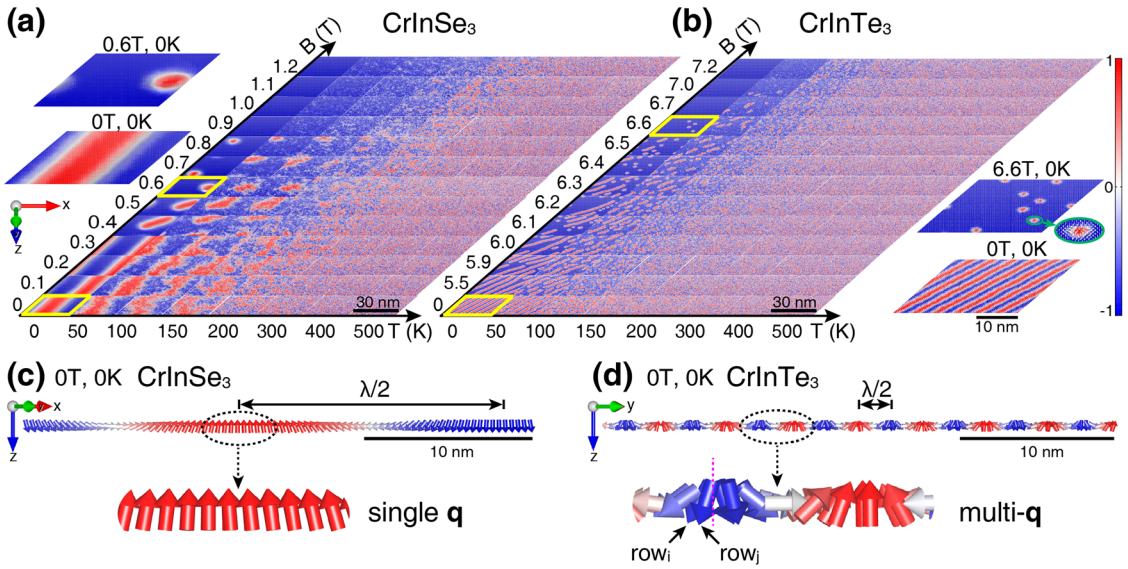

Fig. 6 | Magnetic structures as a function of temperature and magnetic field. Calculated B-T phase diagrams of **a** $CrInSe_3$ and **b** $CrInTe_3$. Two insets are shown in each, representing typical zoomed-up magnetic configurations in phase diagrams (as indicated by yellow parallelograms). Moment orientations are indicated by a heat bar at the right side panel, where blue, white, and red represent the moment that is polarized along +z, in xy-plane, and -z, respectively. **c**, **d** Side views of two 0K, 0T magnetic configurations, along with their specific coordinate vectors. Zoomed-in images illustrate the single **q** spin spiral structure in $CrInSe_3$ and the multi-**q** spin spiral structure in $CrInTe_3$. Relevant length scales are inserted at the bottom right corners of each panel.

that the D/J ratio changes from 0.10 to 0.39 in Se- and Te-based compounds, the difference observed here is expected.

The stripe-like magnetic state evolves under the influence of an external magnetic field and temperature. As the magnetic field increases, the stripe width decreases slowly. The stripe orientation in $CrInSe_3$ may also change due to the need for width adjustment. When the field reaches a threshold, the stripe texture breaks and skyrmions are created. Due to the variation of the magnetic parameters in two compounds, the thresholds are different (0.4 T and 5.5 T for $CrInSe_3$ and $CrInTe_3$, respectively). As the magnetic field keeps increasing, skyrmions change their shape from elliptical to circular. Taking $CrInSe_3$ as an example, the major axis of the ellipses at 0.4 and 0.5 T are 27.8 nm and 25.3 nm, respectively. As the field changes from 0.6 to 0.8 T, the diameter of the circular skyrmion shrinks from 12.02 nm to 8.24 nm. Finally, when the magnitude of the field exceeds 0.9 T, the topological protection of the swirling spin state is destroyed, resulting in an FM state. The overall process for $CrInTe_3$ is similar, but with a more than seven times stronger critical magnetic field, and a much denser of stripes and skyrmions, as a result of the bigger D/J ratio. Interestingly, the evolution of the morphology of these magnetic structures is directly connected to the anisotropic DMI pattern. In specific, along the diagonal direction, which features two relatively larger DMI vectors, a spin stripe phase is formed. This anisotropy remains robust upon the formation of a skyrmion under an external magnetic field, resulting in an elliptical magnetic skyrmion with its semimajor axis aligned along the mirror plane, as shown in Fig. 6a and Supplementary Fig. 8d. This phenomenon is consistent with the recently theoretically predicted elliptical antiskyrmion in monolayer CrI_3[46].

Different from external magnetic fields, limited temperature introduces thermal perturbations into the system, thereby diminishing the correlations between the spin pairs. As can be seen in Fig. 6, with increasing temperature, the spin fluctuation initially occurs at the edge of the periodic spin stripe and the topological skyrmions state. Subsequently, penetrating deeper into these phases and ultimately destroys both long- and short-range spin orders, leading to a paramagnetic phase. The critical temperatures for destroying the spin texture in $CrInSe_3$ and $CrInTe_3$ are approximately 200 K and 150 K. Primarily because the J_1 in $CrInSe_3$ being more than 1.5 times larger than in $CrInTe_3$.

The above-mentioned macroscopic magnetic properties, observed under various external perturbations, are results that reflect the competitive nature of the systems from an energy perspective. More specifically, two aspects of the competitions can be classified as: first, a stability competition among different topological magnetic states; second, the significance of various terms in the spin Hamiltonian (Eq. (4)). As shown in Supplementary Fig. 11, the energy differences of various spin states at specific magnetic fields clearly illustrate the first competition. For instance, increasing the magnetic field from 0.5 T to 0.6 T helps resolve the competition among multiple configurations (60° stripe, 60° + 1 skyrmion, and 30° 1 skyrmion), stabilizing the 1 skyrmion state. This results in a phase transition from the 60° stripe state to the 1 skyrmion state. On the other hand, the latter competition is fundamentally more important, as it rises from terms used to characterize magnetic features, which in turn directly determine the equilibrium state under each set of external conditions. To be specific, each term in the spin Hamiltonian responds to an external field by varying its contribution to the total energy. As it is shown in Fig. 7, the total energy decreases as the magnetic field increases, with the primary positive contributions coming from E_{Ex}, E_{Zeeman}. E_{Ani} shows a similar but more moderate trend. On the contrary, the magnitude of the energy contribution from the DM interaction decreases as a function of the magnetic field. By investigating only the ground state configurations, we found that the emergence of skyrmions requires significant contributions from both E_{DMI} and E_{Zeeman}. Specifically, when the magnetic field is weaker than 0.3 T, the energy contribution of the Zeeman term becomes negligible. Similarly, when the magnetic field is stronger than 0.9 T, the contribution of the DM term becomes unimportant. When the applied magnetic field lies between 0.3 and 0.9 T, the two terms exhibit contrasting variations and compete with each other. In fact, the relative magnitude of these two terms is the decisive factor in determining the skyrmion's morphology. When the DM interaction has a substantial significant role, it results in an elliptical form, whereas when the Zeeman term is more dominant, the skyrmion forms a well-defined swirling configuration.

Adiabatic spin wave spectrum for $CrInX_3$ (X=Se, Te), corresponding to the collinear FM state under a high external magnetic field and the spin spiral ground state with zero external fields, are obtained by adopting the adiabatic approach. As it is shown in Fig. 8, some general features can be observed from the FM spectra. First, the spin waves of the two materials

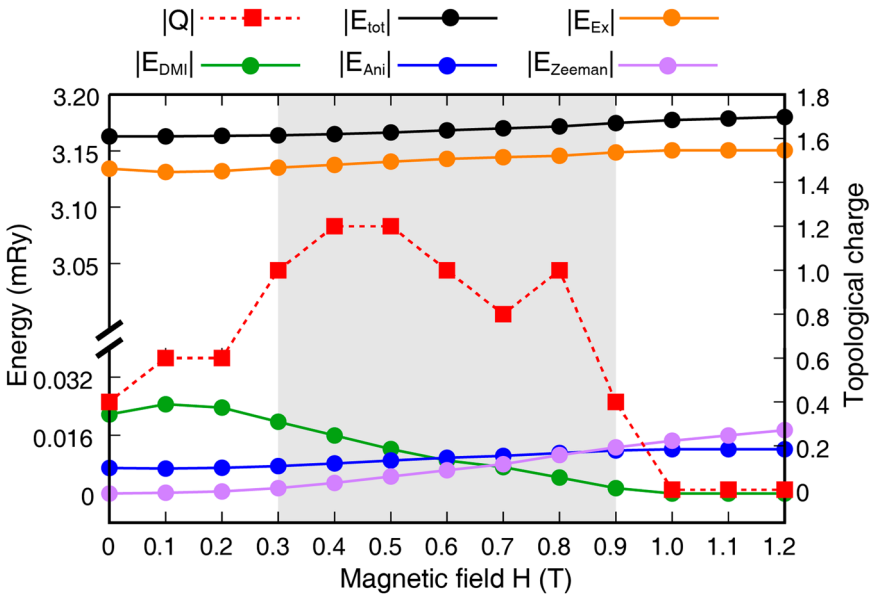

Fig. 7 | Average topological charge, total energies, and decomposed energies of the spin Hamiltonian for $CrInSe_3$ as functions of the external field. The shaded area indicates the magnetic field range where there exists skyrmion(s) in the ground state.

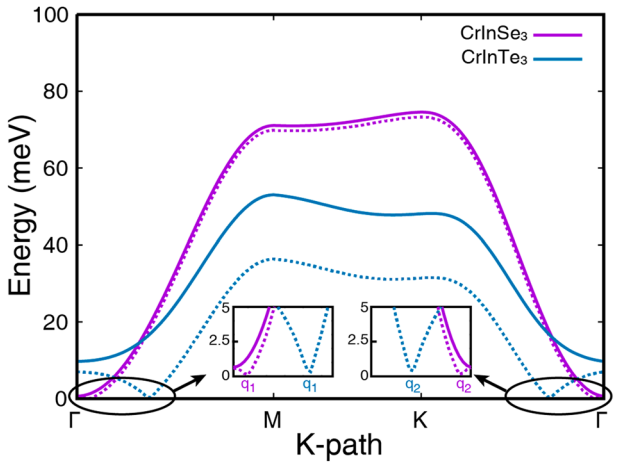

Fig. 8 | Calculated adiabatic spin wave spectrum for $CrInX_3$ (X=Se, Te). Solid and dashed lines represent results obtained from their FM and ground state stripe states, respectively.

exhibit different maximum excitation values, which reflect the difference in overall magnetic interaction strength, more specifically, the dominant exchange parameter J_1. Second, the spin waves of both materials exhibit a quadratic dependence around the Γ point, consistent with the FM ordering adopted in the calculation. Moreover, the magnon softening observed in $CrInTe_3$ indicates a stronger instability, and therefore, a greater tendency toward a non-collinear state. This is verified by the ground state macroscopic spin textures obtained in the Monte Carlo simulations, which reveal a significantly larger spin-spiral propagation vector. Third, the energy gaps at the Γ point for the two systems are 0.66 and 9.70 meV, respectively, representing the threshold energy required to excite each material. It directly reflects the MAE of 0.17 meV for $CrInSe_3$ and 2.43 meV for $CrInTe_3$.

On the other hand, the magnon spectrum of the spin spiral ground state reveals several interesting features attributed to its noncollinear nature. To begin with, the previously lowest energy point in the spectrum has shifted away from the Γ points, which represent the FM state, to a point located within the first Brillouin zone, corresponding to the spin stripe texture. Specifically, as shown in Fig. 8, the dips exhibited by Se- and Te-based compounds along the $\Gamma - M$ path are [0.036,0,0] and [0.188,0,0], respectively. They represent the propagation vectors in that particular direction, with the magnitude providing insights into the spin spiral modulation period. The bigger the period, the smaller the magnitude. Moreover, this magnitude varies along different high symmetry paths, as demonstrated by the vectors [0.188,0,0] along $\Gamma - M$ and [0.096,0.096,0] along $\Gamma - K$ for $CrInTe_3$, respectively. This variation is due to the fact that the spin spiral propagation vector in a real material typically does not align with any high-symmetry directions within the first Brillouin zone. Therefore, a combination of multiple vectors is required for accurate representation. Following this shift, the threshold for exciting specific spin textures in $CrInSe_3$ has been reduced from 0.66 meV to 0.11 meV, and for another compound, from 9.70 meV to 0.34 meV. And the maximum eigenvalue for these compounds has been reduced by 1.27 meV and 16.65 meV, respectively. Last but not least, the spin-stripe texture breaks time-reversal symmetry due to the fact that dip positions, which used to be equivalent, now exhibit non-degeneracy, with each showing different vector magnitudes as well as distinct gap values. As demonstrated in a more detailed spin wave spectrum shown in Supplementary Fig. 13.

Complex ferroelectric polarization properties

Similar to In_2Se_3[41–43], which exhibits excellent room-temperature ferroelectricity due to the displacement of its middle-layer Se atoms, the middle layer of X atoms in $CrInX_3$ is also displaced from its high-symmetry position following the same pattern. The systems are polar due to uncompensated dipole moments originating from Cr-X, and X-In polar bonds. As shown in the inset of Fig. 9a, the spontaneous polarized state corresponds to a structure in which the X atom is positioned directly under the In atom. In contrast, the reference structure aligns with the one that the X atom is located at the midpoint between the Cr and In atoms. This displacement is along [−0.84 0.84 0.27] direction, associated with a polarization of 13.19 $\mu C/cm^2$ for $CrInSe_3$ and 7.38 $\mu C/cm^2$ for $CrInTe_3$, respectively, along the exact same direction. Further investigation shows that the electronic contribution denotes a polarization that is along the displacement direction, while the ionic contribution is along the opposite direction with a slightly weaker value. The total polarization results from the counterbalance between these two contributions, as the detailed data shown in Supplementary Table 7 and Supplementary Fig. 14. Nonetheless, the uncompensated polar bonds between Cr-X and In-X are more pronounced as compared to the case in In_2Se_3 implying larger polarization values in our systems.

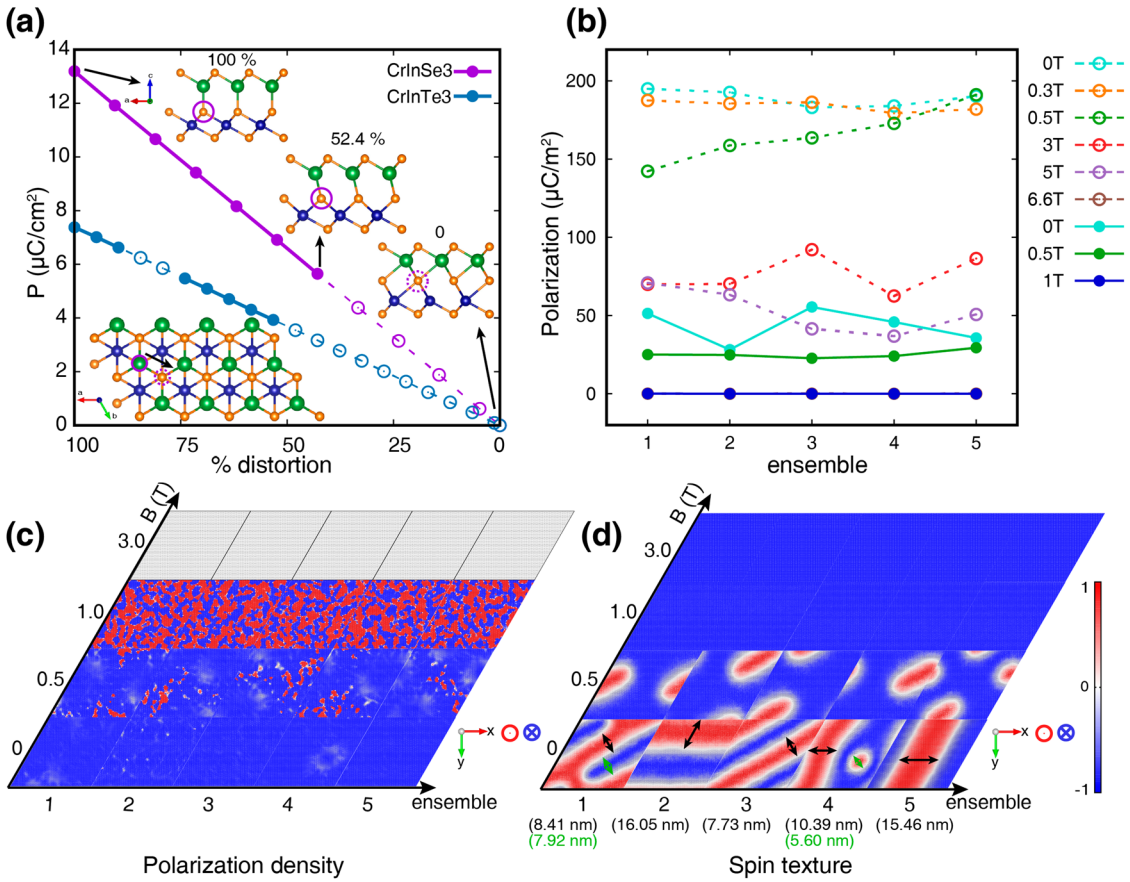

Fig. 9 | Electric polarization. a Calculated ferroelectric polarization by using the modern theory of polarization. The data is plotted as a function of *X* atoms displaced from their high-symmetry position. Purple and blue lines represent the results obtained for $CrInSe_3$ and $CrInTe_3$, respectively. Data denoted by solid (empty) points are the results of calculation (fitting). Insets are the side and top views of the crystal structure with different *X* displacements. Purple solid and dashed circles illustrate the position of the displaced *X* atom. Black arrow in the lower inset indicates the displacement direction. **b** Calculated spin-spiral induced polarization for five magnetic ensembles. Solid and dashed lines represent the results for $CrInSe_3$ and $CrInTe_3$, respectively. Different line colors correspond to the results obtained from various external magnetic fields, ranging from 0 to 6.6 T. **c** Polarization density and **d** the corresponding spin texture of the five ensembles, obtained from $CrInSe_3$. Double-headed arrows colored in black and green denote the spin stripe width and skyrmion diameters.

Except for the polarization induced by the ionic displacement and the corresponding electronic charge redistribution, cycloidal spiral spin state-induced electric polarization plays a surprisingly important role in such material. According to the KNB model, polarization occurs when the spin spiral propagation vector **q** and spin rotation axis **e** form a non-zero angle, and reach its maximum when the angle is equal to 90°. The orientation of the propagation vector **q** is closely related to the chirality of the spin spiral's evolution, as discussed in the computational details in Section "Ferroelectric polarization calculations". In $CrInX_3$, both the spin stripe and the magnetic skyrmions exhibit as Néel-type. As can be seen in Supplementary Fig. 15, both **q** and **e** are orientated within the *xy*-plane and, more importantly, are nearly perpendicular to each other. This configuration makes them ideal candidates for this form of polarization.

To clarify the dependency of ferroelectric polarization on magnetic texture, magnetic structures for each compound are selected under several representative external magnetic fields, with five ensembles examined for each field. The calculated total and projected polarization results are shown in Fig. 9b and Supplementary Fig. 16. First and foremost, the magnitude of the total polarization, P_{tot}, is primarily attributed to its P_z component. This result is perfectly consistent with the one derived from the KNB model, as both **q** and **e** align in-plane, the induced polarization **P**, which is a product of the two, points out-of-plane. Secondly, there is a one-to-one correlation between polarization density and the corresponding spin texture, suggesting the strong interplay between their electric polarization and magnetic characteristics. Take $CrInSe_3$ as an example, when the magnetic structure exhibits a perfect long-range spiral texture, as seen in Fig. 9d at B equal to 0 T, a strong average polarization value of 50 μC/m^2 is observed (indicated by the cyan solid line in Fig. 9b). With increasing external fields, the long-range spiral state is destroyed, transforming into a short-range ordered skyrmion state. This change is directly reflected in the polarization value, as the average drops to 25 μC/m^2 (shown by the green solid line). When the magnetic field is strong enough to disrupt the previously stabilized cycloidal state, an approximate collinear FM state occurs at 1.0 T, where spins are nearly aligned with the magnetic field, deviating by less than six degrees (illustrated in Supplementary Fig. 17). As shown in Fig. 9, the polarization disappears due to a phase transition from the long-range spin spiral state to the approximate collinear FM state. This is reflected in the polarization density, which changes from a purely out-of-plane ordered state (blue) to a randomly distributed state, where clockwise (blue) and anticlockwise (red) spin deviations from the easy axis. With the external magnetic field further increasing to 3.0 T, the noncollinear character disappears (**q** = 0, as there is no spin spiral propagation), and the system becomes strictly FM, thereby resulting in a non-polar state (white). As a result, the system exhibits an interesting series of phase transitions under an increasing magnetic field, starting with the ferroelectric phase, transitioning through the paraelectric phase, and ultimately reaching the non-polar phase. As the total polarization value is the sum of the polarization densities at each lattice site, a more

detailed analysis of the magneto-electric coupling can be obtained by comparing the spin textures with their corresponding polarization densities.

For the spin spiral states, in addition to having the largest polarization values in general, variations in texture, such as stripe width and stripe angle, also affect their polarization outcomes. According to Eq. (5), changes in the magnitude of **q** and the relative angle between **q** and **e** can affect the polarization value. A narrower spin stripe, being represented by a larger propagation vector, consequently generates a larger polarization. For example, a spin stripe with a width of 15.46 nm corresponds to a polarization value of 35.67 $\mu C/m^2$, and one that is 7.73 nm wide corresponds to a polarization of 55.42 $\mu C/m^2$. Moreover, the relatively lower polarization of ensemble 2 is ascribed not only to a wider spin stripe (16.05 nm) but also to a non-90° angle between **q** and **e**, as depicted in Supplementary Fig. 15. When it comes to magnetic skyrmions, the polarization density exhibits a white area around the skyrmion boundary, as it is clearly seen in ensemble 4 at B=0 T. It happens because of the swirling nature of skyrmions: for any spin along a spin spiral chain across the magnetic skyrmion center, the resulting wave vectors always point toward the center. More fundamentally, as the origin of this type of polarization can be traced to the ionic displacement induced by the non-collinear spin structure (referred to as the inverse DM effect)[47,48]. Consequently, one can anticipate variations in the ionic displacement corresponding to this specific circular polarization density. Such realizations pave the way for the emergent formation of a ferroelectric skyrmion, which in itself represents a novel entity in the field of spintronics. With an increasing magnetic field, smaller skyrmions emerge alongside an enlarged FM area. In this case, the characteristic of polarization density is an increase in the white region, accompanied by a randomly interspersed distribution of red and blue areas that represent upward (red) and downward (blue) polarization, respectively. As a result, this leads to a reduction in polarization.

The results obtained for $CrInTe_3$ are similar, while its polarization value, as indicated by the peak of 194.93 $\mu C/m^2$ shown in Fig. 9b, not only more than four times bigger than the $CrInSe_3$ but also significantly exceeds those of the most promising candidates previously identified with this mechanism for type-II multiferroic applications[21]. This phenomenon in $CrInX_3$ not only demonstrates the direct magneto-electric nature but also, more importantly, unveils the potential of controllable magnetoelectric multiferroic skyrmions within a defined magnetic field range.

In summary, the magnetic features of the Janus material $CrInX_3$ (X=Se, Te) were first extracted from first-principles simulations. Based on these, the exchange mechanisms of both Heisenberg and Dzayaloshinskii-Moriya interactions have been fully explained. Two intriguing aspects have been identified: firstly, the unusual e_g electron occupation in Cr-d orbitals, which determines the exchange pathway and, consequently, the related FM and AFM exchange couplings. Secondly, the surprising variation in spin-orbit coupling strength on different X layers, which dictates the orientations of the 3D Dzayloshinskii-Moriya vectors and, therefore, the non-collinear inclination of the spin system. Additionally, detailed phase diagrams have been obtained, from which the importance of E_{DMI} and E_{Zeeman} in the spin Hamiltonian have been emphasized, the mechanisms of magnetic skyrmion formation as well as the decisive factors affecting the swirling shape have been established. Together with magnetic excited states fully exemplified by investigating spin wave spectrum, a complete description of magnetic properties has been achieved. Moreover, further polarization studies have shown that these Janus structures not only exhibit well-defined in-plane polarization but also possess surprisingly high out-of-plane polarization induced by spin spirals. More importantly, by investigating the direct correlation between spin textures and polarization densities, we conclude that multiferroic skyrmions are expected to be observed in experiments. Together with their high magnetic transition temperatures, the $CrInX_3$ compounds emerge as perfect candidates for overcoming the main limiting factors of the multiferroic materials and therefore, pave the way for the discovery of room-temperature, strong magnetoelectric materials for spintronic applications.

Methods

Density functional theory (DFT) based calculations are performed to study the structural, electronic, magnetic, and electric polarization of $CrInX_3$ systems. The structural model was built with a 20 Å vacuum layer along z direction. A $2\times2\times1$ supercell is employed to simulate structures with different magnetic states. The generalized gradient approximation (GGA)[49] is used to take into account the exchange-correlation effect in our density functional theory calculations[50,51]. The strong correlation effect on Cr d-electrons is corrected by adopting the on-site Hubbard U_{eff}[52,53] with a value of 3 eV, which is proven to be good for the Cr-based compounds[54]. All geometry optimization and standard electronic property calculations were carried out using the Vienna ab initio Simulations Package (VASP), a plane wave basis set and projector-augmented wave (PAW)[55,56] code. The kinetic energy cutoff of the plane waves is set to 520 eV. A k-mesh integration is chosen as $9\times9\times1$ and $15\times15\times1$, with the convergence criteria of 1×10^{-6} eV atom^{-1} and 0.005 eV Å^{-1} for the two calculations, respectively.

Magnetic parameters calculations

Furthermore, utilizing the magnetic force theorem and the Lichtenstein-Katsnelson-Antropov-Gubanov (LKAG) formula[57], a complete rank-2 exchange matrix is obtained, from which both the orbital-decomposed isotropic Heisenberg exchange J and the Dzyaloshinskii-Moriya vector $\mathbf{D}_{ij}$[58] can be numerically derived, as implemented in the full-potential linear muffin-tin orbital (FP-LMTO) electronic structure code RSPt[59]. The validity of using the Heisenberg model in this system has been further exemplified, as detailed in Supplementary Note 2. The generalized Heisenberg model is written as

$$H=-\sum_{i\neq j}J_{ij}^{\alpha\beta}\mathbf{e}_i^{\alpha}\mathbf{e}_j^{\beta},\quad \{\alpha,\beta=x,y,z,\} \tag{1}$$

where the unit vectors **e** are the direction of local spins, and the inter-site exchange matrix $\hat{J}_{ij}$ has the following form,

$$\hat{J}_{ij}=\begin{pmatrix} J^{xx} & J^{xy} & J^{xz}\\ J^{yx} & J^{yy} & J^{yz}\\ J^{zx} & J^{zy} & J^{zz}\end{pmatrix}, \tag{2}$$

in which the diagonal components represent isotropic Heisenberg exchange and the DM vector can be written in the form of off-diagonal components, e.g., z component:

$$D_{ij}^{z}=(J_{ij}^{xy}-J_{ij}^{yx})/2. \tag{3}$$

Spin Hamiltonian model

By using the magnetic parameters extracted from the firs-principles calculations mentioned above, the following effective spin Hamiltonian is formulated,

$$\begin{aligned}\mathcal{H}_{\mathrm{eff}}=\ & -\sum_{i,j}J_{ij}\,\mathbf{e}_i\cdot\mathbf{e}_j-\sum_{i,j}\mathbf{D}_{ij}\cdot\left(\mathbf{e}_i\times\mathbf{e}_j\right)\\ & -\sum_i K_i\left(\hat{\mathbf{e}}_i\cdot\mathbf{e}_i^{K}\right)^2-\sum_i\mathbf{B}^{ext}\cdot\mathbf{e}_i\end{aligned} \tag{4}$$

where the third and fourth terms represent energies induced by single-ion anisotropy and external magnetic field, respectively.

Classical Monte Carlo simulations

In this way, the equilibrium magnetic state under any thermal and magnetic field perturbation can be obtained by performing classical Monte Carlo simulations, and the excited spectrum can be achieved by having Fourier transformation of real space parameters or by analyzing dynamic structure factors obtained in spin dynamics simulations. In the simulations, a lattice size of $80 \times 80 \times 1$ is used with an additional consideration of periodicity in the xy-plane, which corresponds to an area of 31.2 nm × 31.2 nm.

Ferroelectric polarization calculations

Electric polarization originating from three sources ionic, electronic, and non-collinear spin texture is calculated separately. Among them, the first two parts are calculated by using the modern theory of polarization[60–63], and the last one is obtained by adopting the approach proposed by Katsura et al.[64], which is equivalent to the Mostovoy's expression[48,65]

$$\mathbf{P} = c\,(\mathbf{e} \times \mathbf{q}), \tag{5}$$

where $c = \gamma\,\chi_e$, with γ stands for the spin-orbit coupling strength and χ_e denotes the dielectric susceptibility. $\mathbf{q}$ is the wave vector of the spiral, and $\mathbf{e} \sim \mathbf{e}_i \times \mathbf{e}_j$ is the spin rotation axis. In $CrIn X_3$, γ is complex due to the varying nature of spin-orbit coupling strengths introduced by ligand atom X, as illustrated in Fig. 5b. On the other hand, there is a lack of experimental data regarding dielectric susceptibility. Therefore, we have chosen c as a constant value of 1 in all of our polarization calculations. It is exemplified by the fact that $\mathbf{e}$ and $\mathbf{q}$ alone sufficiently reflect the significant differences in polarization between the two systems. Therefore, we believe that the approximation of $c = 1$ is adequate to capture the main features of the system.

The wave vector $\mathbf{q}$ is a quantity that represents information on the spin spiral, including both its propagation directions as well as the propagation modulus. The orientation of the wave vector is defined in close relation to the chirality of the spin spiral's evolution[65], as shown in the schematic picture in Supplementary Fig. 18a. Specifically, when the spin spiral evolves clockwise, the wave vector $\mathbf{q}$ is oriented in the same direction; when it evolves anticlockwise, $\mathbf{q}$ is oriented in the opposite direction, as illustrated in Supplementary Fig. 18c, d. In order to take into account the average effect, five layers of nearest neighbors are considered for each site i, comprising a total of 32 j-atoms.

Topological charge calculations

In addition, to quantitatively describe the topological properties of magnetic textures, topological charge Q is calculated by the following formula[66]:

$$Q = \frac{1}{4\pi}\int \mathbf{m} \cdot \left(\frac{\partial \mathbf{m}}{\partial x} \times \frac{\partial \mathbf{m}}{\partial y}\right) \mathrm{d}x\,\mathrm{d}y. \tag{6}$$

Data availability

The data that support the results of this study are available from the corresponding author upon reasonable request.

Code availability

The structural optimizations are performed using `VASP`. The full-potential LMTO code `RSPt` was used to compute the magnetic and electronic properties. The Monte Carlo simulations and non-collinear spin-induced polarizations are performed using the `UppASD` code. All these packages or codes are commercially/freely available. The code used for the topological charge calculations was programmed by our research group and is available from the corresponding authors upon reasonable request.

Received: 29 February 2024; Accepted: 18 July 2024;
Published online: 02 August 2024

References

1. Kanazawa, N., Seki, S. & Tokura, Y. Noncentrosymmetric magnets hosting magnetic skyrmions. *Adv. Mater.* **29**, 1603227 (2017).
2. Yu, X. et al. Biskyrmion states and their current-driven motion in a layered manganite. *Nat. Commun.* **5**, 3198 (2014).
3. Yu, X. et al. Transformation between meron and skyrmion topological spin textures in a chiral magnet. *Nature* **564**, 95–98 (2018).
4. Shinjo, T., Okuno, T., Hassdorf, R., Shigeto, K. & Ono, T. Magnetic Vortex Core Observation in Circular Dots of Permalloy. *Science* **289**, 930–932 (2000).
5. Göbel, B., Mertig, I. & Tretiakov, O. A. Beyond skyrmions: Review and perspectives of alternative magnetic quasiparticles. *Phys. Rep.* **895**, 1–28 (2021).
6. Jonietz, F. et al. Spin transfer torques in MnSi at ultralow current densities. *Science* **330**, 1648–1651 (2010).
7. Jiang, W. et al. Direct observation of the skyrmion Hall effect. *Nat. Phys.* **13**, 162–169 (2017).
8. Everschor, K. et al. Rotating skyrmion lattices by spin torques and field or temperature gradients. *Phys. Rev. B* **86**, 054432 (2012).
9. Jiang, W. et al. Blowing magnetic skyrmion bubbles. *Science* **349**, 283–286 (2015).
10. Zhang, H. et al. Magnetic skyrmions: Materials, manipulation, detection, and applications in spintronic devices. *Mater. Futures* **2**, 032201 (2023).
11. Miron, I. M. et al. Perpendicular switching of a single ferromagnetic layer induced by in-plane current injection. *Nature* **476**, 189–193 (2011).
12. He, B. et al. All-electrical 9-bit skyrmion-based racetrack memory designed with laser irradiation. *Nano Lett.* **23**, 9482–9490 (2023).
13. Spaldin, N. A. & Fiebig, M. The renaissance of magnetoelectric multiferroics. *Science* **309**, 391–392 (2005).
14. Fiebig, M. Revival of the magnetoelectric effect. *J. Phys. D: Appl. Phys.* **38**, R123 (2005).
15. Picozzi, S., Yamauchi, K., Sanyal, B., Sergienko, I. A. & Dagotto, E. Dual nature of improper ferroelectricity in a magnetoelectric multiferroic. *Phys. Rev. Lett.* **99**, 227201 (2007).
16. Hill, N. A. Why are there so few magnetic ferroelectrics? *J. Phys. Chem. B* **104**, 6694–6709 (2000).
17. Sergienko, I. A. & Dagotto, E. Role of the Dzyaloshinskii-Moriya interaction in multiferroic perovskites. *Phys. Rev. B* **73**, 094434 (2006).
18. Hubert, A. & Schäfer, R. *Magnetic domains: the analysis of magnetic microstructures* (Springer Science & Business Media, 1998).
19. Kézsmárki, I. et al. Néel-type skyrmion lattice with confined orientation in the polar magnetic semiconductor GaV_4S_8. *Nat. Mater.* **14**, 1116–1122 (2015).
20. Seki, S., Yu, X., Ishiwata, S. & Tokura, Y. Observation of skyrmions in a multiferroic material. *Science* **336**, 198–201 (2012).
21. Seki, S., Ishiwata, S. & Tokura, Y. Magnetoelectric nature of skyrmions in a chiral magnetic insulator Cu_2OSeO_3. *Phys. Rev. B* **86**, 060403 (2012).
22. Liu, C., Ren, W. & Picozzi, S. Spin-chirality-driven multiferroicity in van der Waals monolayers. *Phys. Rev. Lett.* **132**, 086802 (2024).
23. Heinze, S. et al. Spontaneous atomic-scale magnetic skyrmion lattice in two dimensions. *Nat. Phys.* **7**, 713–718 (2011).
24. Garlow, J. A. et al. Quantification of mixed Bloch-Néel topological spin textures stabilized by the Dzyaloshinskii-Moriya interaction in Co/Pd multilayers. *Phys. Rev. Lett.* **122**, 237201 (2019).
25. Yu, X. Z. et al. Transformation between meron and skyrmion topological spin textures in a chiral magnet. *Nature* **564**, 95–98 (2018).
26. Zhang, J. et al. Janus monolayer transition-metal dichalcogenides. *ACS Nano* **11**, 8192–8198 (2017).
27. Lu, A.-Y. et al. Janus monolayers of transition metal dichalcogenides. *Nat. Nanotechnol.* **12**, 744–749 (2017).
28. Trivedi, D. B. et al. Room-temperature synthesis of 2D Janus crystals and their heterostructures. *Adv. Mater.* **32**, 2006320 (2020).

29. Guan, Z. et al. Two-dimensional Janus polarization functioned by mechanical force. *Adv. Mater.* **36**, 2403929 (2024).
30. Lin, Y.-C. et al. Low energy implantation into transition-metal dichalcogenide monolayers to form Janus structures. *ACS nano* **14**, 3896–3906 (2020).
31. Levoska, J. et al. Pulsed laser ablation deposition of $CuInSe_2$ and $CuIn_{1-x}Ga_xSe_2$ thin films. *Phys. Scr.* **1994**, 244 (1994).
32. Belik, A. A. Polar and nonpolar phases of $BiMO_3$: A review. *J. Solid State Chem.* **195**, 32–40 (2012).
33. Dong, L., Lou, J. & Shenoy, V. B. Large in-plane and vertical piezoelectricity in Janus transition metal dichalchogenides. *ACS nano* **11**, 8242–8248 (2017).
34. Liang, J. et al. Very large Dzyaloshinskii-Moriya interaction in two-dimensional Janus manganese dichalcogenides and its application to realize skyrmion states. *Phys. Rev. B* **101**, 184401 (2020).
35. Xu, C. et al. Topological spin texture in Janus monolayers of the chromium trihalides $Cr(I, X)_3$. *Phys. Rev. B* **101**, 060404 (2020).
36. Yuan, J. et al. Intrinsic skyrmions in monolayer Janus magnets. *Phys. Rev. B* **101**, 094420 (2020).
37. Cui, Q., Liang, J., Shao, Z., Cui, P. & Yang, H. Strain-tunable ferromagnetism and chiral spin textures in two-dimensional Janus chromium dichalcogenides. *Phys. Rev. B* **102**, 094425 (2020).
38. Chen, Y., He, J., Wang, S., Feng, Y. P. & Zhou, J. Tuning the magnetic and electronic properties of two-dimensional electrides by forming cationic Janus compounds. *J. Alloy. Compd.* **930**, 167417 (2023).
39. Du, W. et al. Spontaneous magnetic skyrmions in single-layer $CrInX_3$ (X= Te, Se). *Nano Lett.* **22**, 3440–3446 (2022).
40. Sun, Z. et al. Intrinsic bitunable magnetism/polarity behavior in 2D Janus $Cr_2I_3Y_3$ (Y= F, Cl, or Br) systems. *npj 2D Mater. Appl.* **6**, 69 (2022).
41. Ding, W. et al. Prediction of intrinsic two-dimensional ferroelectrics in In_2Se_3 and other III_2-VI_3 van der waals materials. *Nat. Commun.* **8**, 14956 (2017).
42. Zhou, Y. et al. Out-of-plane piezoelectricity and ferroelectricity in layered α-In_2Se_3 nanoflakes. *Nano Lett.* **17**, 5508–5513 (2017).
43. Zheng, C. et al. Room temperature in-plane ferroelectricity in van der waals In_2Se_3. *Sci. Adv.* **4**, eaar7720 (2018).
44. Wang, D. & Sanyal, B. Systematic study of monolayer to trilayer CrI_3: stacking sequence dependence of electronic structure and magnetism. *J. Phys. Chem. C.* **125**, 18467–18473 (2021).
45. Moriya, T. Anisotropic superexchange interaction and weak ferromagnetism. *Phys. Rev.* **120**, 91–98 (1960).
46. Huang, K., Schwartz, E., Shao, D.-F., Kovalev, A. A. & Tsymbal, E. Y. Magnetic antiskyrmions in two-dimensional van der waals magnets engineered by layer stacking. *Phys. Rev. B* **109**, 024426 (2024).
47. Sergienko, I. A. & Dagotto, E. Role of the dzyaloshinskii-moriya interaction in multiferroic perovskites. *Phys. Rev. B* **73**, 094434 (2006).
48. Khomskii, D.*Transition metal compounds* (Cambridge University Press, 2014).
49. Perdew, J. P., Burke, K. & Ernzerhof, M. Generalized gradient approximation made simple. *Phys. Rev. Lett.* **77**, 3865 (1996).
50. Kohn, W. & Sham, L. J. Self-consistent equations including exchange and correlation effects. *Phys. Rev.* **140**, A1133 (1965).
51. Kresse, G. & Furthmüller, J. Efficient iterative schemes for ab initio total-energy calculations using a plane-wave basis set. *Phys. Rev. B* **54**, 11169 (1996).
52. Anisimov, V. I., Aryasetiawan, F. & Lichtenstein, A. First-principles calculations of the electronic structure and spectra of strongly correlated systems: the LDA+U method. *J. Phys.: Condens. Matter* **9**, 767 (1997).
53. Dudarev, S. L., Botton, G. A., Savrasov, S. Y., Humphreys, C. & Sutton, A. P. Electron-energy-loss spectra and the structural stability of nickel oxide: An LSDA+U study. *Phys. Rev. B* **57**, 1505 (1998).
54. Kashin, I. V., Mazurenko, V. V., Katsnelson, M. I. & Rudenko, A. N. Orbitally-resolved ferromagnetism of monolayer CrI_3. *2D Mater.* **7**, 025036 (2020).
55. Blöchl, P. E. Projector augmented-wave method. *Phys. Rev. B* **50**, 17953 (1994).
56. Kresse, G. & Joubert, D. From ultrasoft pseudopotentials to the projector augmented-wave method. *Phys. Rev. B* **59**, 1758 (1999).
57. Liechtenstein, A. I., Katsnelson, M., Antropov, V. & Gubanov, V. Local spin density functional approach to the theory of exchange interactions in ferromagnetic metals and alloys. *J. Magn. Magn. Mater.* **67**, 65–74 (1987).
58. Udvardi, L., Szunyogh, L., Palotás, K. & Weinberger, P. First-principles relativistic study of spin waves in thin magnetic films. *Phys. Rev. B* **68**, 104436 (2003).
59. Wills, J. M. et al. *Full-Potential Electronic Structure Method: energy and force calculations with density functional and dynamical mean field theory* Vol. 167 (Springer Science & Business Media, 2010).
60. King-Smith, R. D. & Vanderbilt, D. Theory of polarization of crystalline solids. *Phys. Rev. B* **47**, 1651–1654 (1992).
61. Vanderbilt, D. & King-Smith, R. D. Electric polarization as a bulk quantity and its relation to surface charge. *Phys. Rev. B* **48**, 4442–4455 (1993).
62. Resta, R. Macroscopic electric polarization as a geometric quantum phase. *EPL (Europhys. Lett.)* **22**, 133–138 (1993).
63. Spaldin, N. A. A beginner's guide to the modern theory of polarization. *J. Solid State Chem.* **195**, 2–10 (2012).
64. Katsura, H., Nagaosa, N. & Balatsky, A. V. Spin current and magnetoelectric effect in noncollinear magnets. *Phys. Rev. Lett.* **95**, 057205 (2004).
65. Mostovoy, M. Ferroelectricity in spiral magnets. *Phys. Rev. Lett.* **96**, 067601 (2006).
66. Berg, B. & Lüscher, M. Definition and statistical distributions of a topological number in the lattice O(3) σ-model. *Nucl. Phys. B* **190**, 412–424 (1981).

Acknowledgements

We thank Z. Pan and R. M. Vieira for their helpful discussions. This work was supported by the Science and Technology Development Fund from Macau SAR (Grant No. 0062/2023/ITP2) and the Macao Polytechnic University (Grant No. RP/FCA-03/2023). B.S. acknowledges financial support from Swedish Research Council (Grant No. 2022-04309). The computations were enabled in project SNIC 2022/3-30 by resources provided by the Swedish National Infrastructure for Computing (SNIC) at NSC, PDC, and HPC2N partially funded by the Swedish Research Council (Grant No. 2018-05973). W.S. acknowledges the National Key R&D Program of China (No. 2023YFB4005402), Foundation of National Key Laboratory of Shock Wave and Detonation Physics (No. JCKYS2023212004) and the Key Laboratory of Nuclear Physics and Nuclear Technology (No. NLK2022-07) and the Big Data Computing Center of Southeast University for providing the facility support on the numerical calculations. M.S. thanks S.G. and M.J.S. of FMD Group, SRMIST, Chennai, India for useful discussions.

Author contributions

F.Z.: Investigation (lead); Data curation (lead); Formal analysis (equal); Visualization (lead); Writing - original draft (lead). M.S.: Methodology (supporting); Formal analysis (supporting); Writing - review & editing (supporting). W.S.: Writing - review & editing (supporting). F.C.: Investigation (supporting); Visualization (supporting). X.C.: Writing - review & editing (supporting). S.L.: Formal analysis (supporting). H.T.: Formal analysis (supporting). B.S.: Resources (equal); Writing - review & editing (supporting); Supervision (supporting). D.W.: Conceptualization (lead); Resources (equal); Formal analysis (equal); Methodology (lead); Writing - review & editing (lead); Funding acquisition (lead); Supervision (lead).

Competing interests
The authors declare no competing interests.

Additional information
Supplementary information The online version contains supplementary material available at https://doi.org/10.1038/s41699-024-00490-9.

Correspondence and requests for materials should be addressed to Biplab Sanyal or Duo Wang.